PNAS RESEARCH ARTICLE | MEDICAL SCIENCES

Cancer-associated fibroblast-derived SEMA3C facilitates colorectal cancer liver metastasis via NRP2-mediated MAPK activation

Yuyuan Zhang[a,b,c,1], Anning Zuo[a,1], Yuhao Ba[a,1], Shutong Liu[a,1], Jingqi Chen[d], Shuaixi Yang[e], Siyuan Weng[a], Yukang Chen[a], Hui Xu[a], Peng Luo[f], Quan Cheng[g], Bufu Tang[h], Benyu Liu[i], Chuhan Zhang[j], Jingkuan Yang[a], Xinwei Han[a,b,c,2], and Zaoqu Liu[a,b,c,k,2]

Affiliations are included on p. 11.

Edited by Helen Piwnica-Worms, The University of Texas MD Anderson Cancer Center, Houston, TX; received November 6, 2024; accepted April 9, 2025

Liver metastasis remains the predominant cause of mortality in patients with colorectal cancer (CRC). Nevertheless, the mechanisms underlying the initiation of colorectal cancer liver metastasis remain poorly elucidated. During the metastatic process of CRC cells from the primary site to the liver, we performed time-resolved analyses and identified a subset of tumor cells spatially located in the primary tumor and temporally distributed in the early stages of liver metastasis. These cells were termed liver metastasis-initiating cells (LMICs). LMICs exhibit high stemness, low proliferation, active interaction with surrounding stromal components, and a close association with liver metastasis. Notably, we found significant interactions between cancer-associated fibroblasts (CAFs) and LMICs via the SEMA3C–NRP2 receptor–ligand pair. Further in vivo and in vitro experiments confirmed that CAF-secreted SEMA3C could bind to the NRP2 receptor, which activates the MAPK pathway and promotes colorectal cancer liver metastasis. Our findings suggest potential therapeutic strategies for the early prevention of colorectal cancer liver metastasis.

colorectal cancer | liver metastasis | single-cell | metastasis-initiating

Significance

Liver metastasis remains the predominant cause of mortality in patients with colorectal cancer (CRC). Nevertheless, the mechanisms underlying the initiation of colorectal cancer liver metastasis remain poorly elucidated. The cellular origin of colorectal cancer liver metastasis and crosstalk in the tumor microenvironment were elucidated. SEMA3C derived from cancer-associated fibroblasts (CAFs) strongly interacts with tumor cells and promotes colorectal cancer liver metastasis through the SEMA3C–NRP2 axis. These findings provide insights into the roles of CAFs and CAF-secreted SEMA3C in colorectal cancer liver metastasis, revealing that CAF-secreted SEMA3C interacts with the NRP2 receptor, activates the MAPK-p38/JNK axis, ultimately promotes liver metastasis, and contributes to poor prognosis.

Colorectal cancer liver metastasis, one of the leading causes of death in colorectal cancer (CRC) patients, contributes to a significant global burden due to high mortality and poor prognosis (1). Tumor metastasis is generally related to a subpopulation of cancer cells in the primary site with metastatic properties and complex interactions with the components in the surrounding tumor microenvironment (TME) (2). These cancer cells, characterized by stemness and immune evasion, eventually escape from the primary tumor, acting as "seeds" to colonize distant sites under favorable conditions (3). Consequently, understanding the origin, characteristics, and vulnerabilities of these cells within their niche ecosystems is critical for developing strategies to improve the prevention and treatment of metastasis. Advances in single-cell RNA sequencing (scRNA-seq) technology have enabled high-resolution investigation of metastatic evolution (4). Prior studies have identified lung cancer cell subpopulations with brain-metastatic tropism (5), along with metastasis-initiating ovarian cancer cell clusters acting as metastatic seeds in peritoneal dissemination (6). Despite these advancements, the molecular mechanisms underlying tumor subpopulation-driven colorectal cancer liver metastasis are yet to be fully elucidated.

In recent years, cancer-associated fibroblasts (CAFs) have increasingly garnered attention (7). Through the secretion of various molecules including proteinases and extracellular matrix (ECM) components, CAFs establish metastatic niches that support tumor cell colonization (8). Notably, CAFs produce matrix metalloproteinases (MMPs), key proteolytic enzymes. By degrading ECM components, these enzymes generate a permissive microenvironment that facilitates tumor cell migration and invasion (7). Furthermore, CAFs secrete growth factors like transforming growth factor-beta (TGF-β), which initiates epithelial–mesenchymal transition (EMT). This process confers enhanced migratory and invasive capabilities on tumor cells (9). Additionally, the crosstalk between CAFs and other cellular components within the TME contributes to the establishment of an immunosuppressive milieu or directly induce EMT in tumor cells, ultimately facilitating metastatic progression (10). Nevertheless, the regulatory mechanisms through which CAFs orchestrate early-stage metastatic dissemination remain to be elucidated.

Here, we identified a specific subpopulation of LMICs, characterized by high stemness, low proliferative activity, and significant interactions with stromal components. Mechanistically, our research dissected an intriguing interplay between CAFs and LMICs, demonstrating that SEMA3C secreted by CAFs binds to NRP2 receptors on LMICs,

Author contributions: X.H. and Z.L. designed research; A.Z., Y.B., S.L., J.C., S.Y., S.W., Y.C., H.X., P.L., Q.C., B.T., B.L., C.Z., J.Y., X.H., and Z.L. performed research; Y.Z., X.H., and Z.L. analyzed data; Z.L. designed, conceived, and supervised the research; and Y.Z. wrote the paper.

The authors declare no competing interest.

This article is a PNAS Direct Submission.

Copyright © 2025 the Author(s). Published by PNAS. This article is distributed under Creative Commons Attribution-NonCommercial-NoDerivatives License 4.0 (CC BY-NC-ND).

[1]Y.Z., A.Z., Y.B., and S.L. contributed equally to this work.

[2]To whom correspondence may be addressed. Email: fcchanxw@zzu.edu.cn or liuzaoqu@163.com.

This article contains supporting information online at https://www.pnas.org/lookup/suppl/doi:10.1073/pnas.2423077122/-/DCSupplemental.

Published May 22, 2025.

triggering activation of the MAPK-p38/JNK signaling pathway, which drives liver metastasis and is associated with poor clinical outcomes. These findings elucidate the mechanisms of colorectal cancer liver metastasis and unveil the SEMA3C–NRP2 axis as a druggable target for metastatic interception.

Results

Single-Cell Analysis Reveals a Specific Malignant Cell Cluster in Primary and Liver-Metastatic CRC. Single-cell data from both primary and paired metastatic CRC samples were utilized to perform quality control and cell annotations (Fig. 1*A*). Eleven distinct cell types were identified based on the expression of classical marker genes (Fig. 1 *B*–*D*), and malignant cells were further identified via the InferCNV algorithm (11) (Fig. 1 *E* and *F*). The malignant cells were then reclustered and ultimately classified into four malignant clusters (MC): S100A2+MC1, CST1+MC2, SOX4+MC3, and TFF3+MC4 (*SI Appendix*, Fig. S1). Notably, a significant tissue-specific distribution of malignant cells was observed, and interestingly, TFF3+MC4 comprised cells from both primary and metastatic CRC (Fig. 1*G*). The CytoTRACE analysis (12) positioned that this cluster might exhibit a strong differentiation potential (Fig. 1*H*), which was further corroborated by a similar expression pattern of stem-related genes and signatures (Fig. 1*I*). Notably, TFF3+MC4 was predominantly enriched in terms related to cell motility and adhesion, such as cadherin binding, actin binding, and protein antigen binding, implicating its pivotal role in metastatic progression (Fig. 1*J*). Given the distinct characteristics of TFF3+MC4, we applied pseudotime analysis using the Monocle algorithm (13) to decode the cellular evolutionary dynamics. Along the trajectory, tumor cells showed an increase in aggressive differentiation (Fig. 1 *K*–*M*), reflecting a transition from primary tumor-derived cancer cells to liver metastasis-derived cancer cells. Notably, TFF3+MC4 persisted throughout the pseudotime trajectory, suggesting that TFF3+MC4 cells play an active role in liver metastasis. Spatial transcriptomics analysis and Ro/e analysis (14) confirmed the presence of TFF3+MC4 cells in both primary CRC and liver metastatic sites (Fig. 1 *N*–*O*), consistent with phenotypic plasticity enabling metastatic outgrowth. Clinically, elevated MC4 abundance correlated with reduced overall survival in bulk transcriptomic data (TCGA-CRC, $P = 0.027$; GSE159216, $P = 0.022$) (Fig. 1*P*). Enrichment analysis of genes ranked by their association with TFF3+MC4 scores revealed that the top-ranked genes were predominantly associated with cell adhesion and TGF-β signaling pathways (Fig. 1*Q*).

Identification of Liver Metastasis-Initiating Cells in Primary CRC Tissues. Given that the TFF3+MC4 cells were shared by both primary CRC and liver metastatic tissues, we focused on these cells to dissect the different phases of liver metastasis and aimed to uncover the developmental sequence of tumor cells. Thus, we reclustered TFF3+MC4 (Fig. 2*A*) and employed three algorithms to infer cellular evolutionary trajectories leveraging distinct computational frameworks, including VECTOR (15), Monocle (13), and Slingshot (16). Interestingly, the estimated cell state velocities are consistent with the predicted pseudotemporal order, as the cells within the ellipses of VECTOR plots (Fig. 2*A*). Thus, we defined the cells overlapping in the initial vector field (Fig. 2*A*) and the starting branch of the pseudotime (Fig. 2*B*) as the LMICs in CRC (Fig. 2*C*). Further validation with Slingshot demonstrated the initial segment of the cell evolution trajectory (Fig. 2*D*). Strikingly, as these trajectory scores increased, proliferative capacity (CDCA7 and LEFTY1) increased, while stemness markers (SEMA3F, EREG, and SPHK1) gradually diminished, demonstrating the dynamic changes in proliferative capacity and stemness during the metastatic process of LMICs (Fig. 2*E*). Next, we delineated the biological properties of LMICs, which showed elevated activity in EMT and stemness-related pathways while concurrently displaying reduced activity in the oxidative phosphorylation pathway (Fig. 2*F*). Detailed biological functions are presented in Fig. 2*G*, where tumor-related pathways, such as apical junction, hypoxia, and angiogenesis, were upregulated, whereas cell proliferation-related pathways, such as MYC targets V2, G2M checkpoint, and E2F targets, were downregulated in LMICs. Bulk transcriptomic analysis further supported that a high LMIC score was also linked to superior stemness (Fig. 2*H*). Genes associated with enhanced EMT activation, such as CDH2 and VIM, showed a significant positive correlation with the LMIC score, whereas genes associated with reduced EMT activation, such as CDH1, and the proliferation marker Ki67, displayed a significant negative correlation with the LMIC score (Fig. 2*I*). In TCGA-CRC, patients with high LMIC score exhibited poorer prognoses and a higher propensity for metastasis (Fig. 2*J*). Cox analysis results from five bulk transcriptomic datasets further validated that the high infiltration of the LMIC subset is an unfavorable prognostic factor in CRC (Fig. 2*K*).

Enrichment analysis of different tumor cell subpopulations revealed that LMICs actively interact with the extracellular matrix, as evidenced by pathways involved in cell junction assembly, apical junction, and cell adhesion molecules (Fig. 2*L*). Upregulation of ECM1 and FYN implicated constitutive focal adhesion kinase (FAK) signaling in LMICs (Fig. 2*M*). Mechanistically, LMICs orchestrated FAK-driven invasion via matrix mechanosensing (Fig. 2*N*), coupling ECM receptor interactions with actomyosin contractility. In TCGA-CRC, the stromal score, calculated using the ESTIMATE algorithm, exhibited a stronger correlation with the LMIC score compared to other scores (Fig. 2*O*). Additionally, GSVA scores for the FAK, ECM, and CAM pathways were all significantly positively correlated with LMIC score (Fig. 2*P*). Metastatic lesions exhibited marked upregulation of PTK2 (FAK-encoding) and VEGFA (FAK-regulated) (Fig. 2*Q*), confirming pathway activation in distant metastasis.

SEMA3C+CAFs Display Superior Interactions and Close Proximity to Tumor Cells, Correlated with Liver Metastasis in CRC. To further investigate the intercellular communications between LMICs and other cells in the TME, we performed CellPhoneDB (17) analysis to infer latent cell–cell interactions. Notably, compared to other epithelial cells at the primary site, LMICs exhibited high-intensity interactions with surrounding cells, particularly CAFs (Fig. 3*A*). Spatial transcriptomic profiling demonstrated colocalization of CAF and LMIC cellular signatures (Fig. 3*B*), providing topological evidence for their interactions. Ligand–receptor deconvolution identified SEMA3C–NRP2 axis as the dominant CAF–LMIC communication axis (*SI Appendix*, Fig. S2), mechanistically linking stromal activation to metastatic initiation. Previous studies (18–20) have established SEMA3C as a CAF-derived promigratory factor in pancreatic adenocarcinoma and glioblastoma. Our research further suggested that the interactions between SEMA3C+CAFs and surrounding cells were significantly stronger than those with SEMA3C–CAFs (Fig. 3 *C* and *D*). Functional enrichment analysis indicated that SEMA3C+CAFs were associated with EMT (Fig. 3*E*). Collectively, SEMA3C+CAFs orchestrate tumor cell plasticity and TME remodeling through paracrine signaling. Bulk transcriptomic analysis confirmed strong covariation between SEMA3C+CAF abundance and LMIC scores (Fig. 3*F*). Elevated SEMA3C+CAF scores predicted shorter overall

survival, higher metastatic potential, and advanced tumor stage (Fig. 3 *G*–*I*). Enrichment analysis prioritized integrin-mediated cell adhesion as the central mechanism (Fig. 3*J*).

Next, we calculated the stromal scores and fibroblast scores in 25 CRC cohorts using the ESTIMATE and xCell algorithms and revealed that SEMA3C showed a strong positive correlation with these scores (21) (*SI Appendix*, Fig. S3*A*). A similar trend was observed between CAF-related genes and SEMA3C, validating its predominant localization in the ECM (*SI Appendix*, Fig. S3*B*). Cross-subtype analysis using two published classifications revealed SEMA3C overexpression in the mesenchymal-rich subtypes (22, 23). Notably, consensus molecular subtype 4 (CMS4) and Fibrotic subtype (F) exhibited the highest expression levels of SEMA3C (Fig. 3*K*). Furthermore, in both the GSE39084 and TCGA-CRC cohorts, patients with metastases had significantly higher SEMA3C expression than those without metastases (Fig. 3*L*), and patients with high SEMA3C expression had worse prognoses (Fig. 3*M*). These findings suggest that SEMA3C emerged as a potential marker for liver metastasis and poor outcomes in CRC. To validate these results, we collected primary tumor tissues from CRC patients with and without liver metastases. Immunohistochemistry (IHC) showed significantly stronger staining in patients with liver metastases than in those without (Fig. 3*N*). Furthermore, multiplex immunohistochemistry (mIHC) confirmed that increased SEMA3C expression in liver metastases colocalized with CAFs, and SEMA3C+CAFs were closer to tumor cells compared to SEMA3C–CAFs (Fig. 3*O*).

CAF-Secreted SEMA3C Promotes Liver Metastasis and Poor Prognosis in CRC. To mechanistically validate the prometastatic function of CAF-secreted SEMA3C, we conducted orthogonal functional assays in vitro and in vivo. First, recombinant human (rhSEMA3C) and mouse (rmSEMA3C) proteins were purified to assess direct effects on prometastatic phenotypes. To better mimic CAF-driven influences, primary CAFs isolated from treatment-naïve CRC resections were lentivirally transduced to stably overexpress SEMA3C (CAF–SEMA3C), with empty vector-transduced CAFs (CAF–NC) as controls (*SI Appendix*, Fig. S4 *A* and *B*). ELISA demonstrated that CAF–SEMA3C/CAF–Sema3c secreted significantly higher levels of SEMA3C protein into the liquid supernatant (*SI Appendix*, Fig. S4*C*). Recombinant proteins and conditioned media (CM) from these cells were then used to pretreat SW480 and CT26 cancer cell lines. Compared to the CAF–NC groups, treatment with recombinant SEMA3C proteins and CM from CAF–SEMA3C significantly promoted cell invasion and migration (*SI Appendix*, Fig. S4 *D*–*F* and Fig. 4 *A* and *B*). Western blotting experiments revealed that treated cells exhibited upregulation of mesenchymal-related molecules, including N-cadherin, Vimentin, and ZEB1 proteins, along with downregulation of the epithelial marker E-cadherin (Fig. 4*C* and *SI Appendix*, Fig. S5 *A* and *B*).

Furthermore, the in vivo impact of SEMA3C on CRC progression was examined by coinjecting SW480 cells with either CAF–NC or CAF–SEMA3C into the subcutaneous region of mice to establish subcutaneous tumor models. Notably, the CAF–SEMA3C group exhibited significantly larger tumor volumes and weights compared to the CAF–NC group (Fig. 4*D*). These findings were further corroborated in PDX models, where rhSEMA3C-treated mice showed significantly greater tumor volumes and weights compared to controls (Fig. 4*E*). Next, orthotopic implantation of CT26 cells with either CAF–NC or CAF–Sema3c into the cecum generated spontaneous liver metastases (Fig. 4*F*). Notably, the CAF–Sema3c coinjection developed larger tumors and showed a marked increase in liver metastases (Fig. 4 *F* and *G*). IHC revealed that tumors from the CAF–SEMA3C group exhibited significantly stronger staining for mesenchymal markers such as N-cadherin, Vimentin, Snail, and Zeb1, alongside weaker staining for the epithelial marker E-cadherin (Fig. 4*H* and *SI Appendix*, Fig. S5*C*).

CAF-Secreted SEMA3C Mediates Liver Metastasis via Direct Interaction with NRP2. Prior findings have demonstrated that SEMA3C+CAFs interact with tumor cells via the SEMA3C–NRP2 ligand–receptor axis (*SI Appendix*, Fig. S2). First, we demonstrated that NRP2 (the receptor for SEMA3C) is specifically expressed in LMICs. Notably, an overlapping distribution of NRP2 with LMICs was observed in the UMAP (Fig. 5*A*). Correlation analysis indicated that NRP2 expression is significantly associated with pseudotime and LMIC scores (Fig. 5*B*), a finding validated by bulk RNA-seq data showing elevated LMIC scores in the high-NRP2 group (Fig. 5*C*). Further spatial analysis revealed the widespread and pronounced SEMA3C–NRP2 interaction activities in primary tumor tissues (Fig. 5*D*). Additionally, SEMA3C expression strongly correlated with NRP2 expression (Fig. 5*E*). Coimmunoprecipitation (Co-IP) assays confirmed the specific interaction between SEMA3C and NRP2 (Fig. 5*F*). Clinically, similar to SEMA3C, patients with higher NRP2 expression exhibited poorer prognoses, more advanced tumor stages, and a higher incidence of distant and lymphatic metastases (Fig. 5*G* and *SI Appendix*, Fig. S6). Enrichment analyses revealed that patients with high NRP2 expression exhibited enhanced activation of the EMT pathway (Fig. 5 *H* and *I*). Moreover, NRP2 expression positively correlates with mesenchymal markers (CDH2, VIM) but only weakly with the epithelial marker CDH1 (Fig. 5*J*).

To further validate that SEMA3C promotes liver metastasis via receptor NRP2, we first established stably transfected SW480 and CT26 cell lines using NRP2 shRNA lentiviral particles (*SI Appendix*, Fig. S4*G*). Functional assays in SW480 (*SI Appendix*, Fig. S7 *A* and *C*) and CT26 (*SI Appendix*, Fig. S7 *B* and *C*) cells demonstrated that NRP2 knockdown significantly reversed the enhanced invasive and migratory abilities induced by the recombinant SEMA3C protein or CAF–SEMA3C or CAF–Sema3c CM treatment. In vivo experiments further revealed that tumors derived from shNrp2 cells exhibited markedly reduced growth. While coinjection of CAF–SEMA3C and SW480 cells promoted subcutaneous tumor growth in control mice, NRP2 knockdown significantly reduced tumor size (Fig. 5*K*). In orthotopic models, CAF–Sema3c induced increased tumor volume and high potential of liver metastasis, whereas NRP2 knockdown resulted in significant reductions in tumor size, tumor weight, and the number of liver metastases (Fig. 5 *L*–*O*). IHC analysis of the orthotopic tumors confirmed the reversal of EMT activation following NRP2 knockdown (*SI Appendix*, Fig. S8).

SEMA3C Promotes Liver Metastasis via NRP2-Mediated MAPK Activation. Single-cell analysis revealed NRP2+ malignant cells enriched in functional pathways including focal adhesion, endocytosis, and MAPK signaling (Fig. 6*A*). UMAP analysis demonstrated that the LMIC subset displayed markedly elevated MAPK pathway activity scores (Fig. 6*B*). In alignment with these findings, single-cell analysis showed a strong positive correlation between MAPK pathway activity, NRP2 expression, and EMT pathway activity (Fig. 6*C*). Subsequently, we established orthotopic tumor models by coinjecting CT26 cells with either CAF–NC or CAF–SEMA3C into the cecal wall. After 6 wks, primary tumors were harvested for RNA sequencing (Fig. 6*D* and *SI Appendix*, Fig. S9*A*). Transcriptomic analysis identified pathway activation signatures in the CAF–SEMA3C group, particularly in MAPK signaling, HIF-1α response, and fatty

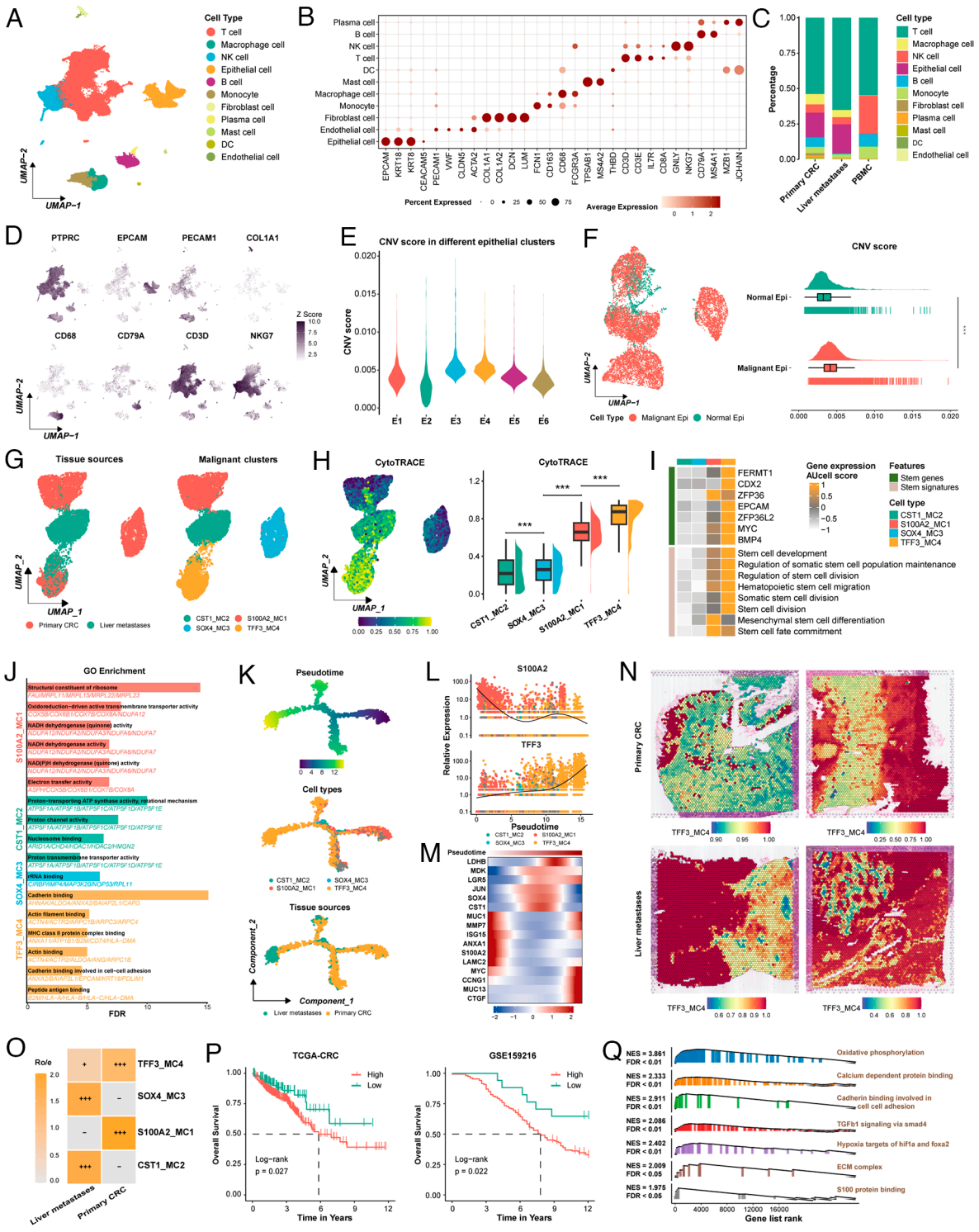


Fig. 1. Single-cell Analysis of CRC and Paired Liver Metastasis Reveals Tumor Heterogeneity. (*A*) Uniform manifold approximation and projection (UMAP) plot showing 11 cell clusters of primary CRC and liver metastatic patients. Cells from different clusters are marked by colors. (*B*) Dot plot showing the expression levels and percentages of classic marker genes across the 11 cell clusters. (*C*) Bar plot showing the percentages of cell types in primary CRC, liver metastasis, and peripheral blood mononuclear cells (PBMCs) samples. (*D*) UMAP plots showing the expression of marker genes (PTPRC, EPCAM, PECAM1, COL1A1, CD68, CD79A, CD3D, and NKG7), colored by gene expression. (*E*) Violin plots showing copy number variation (CNV) scores of six epithelial clusters (E1–E6). (*F*) UMAP plot of epithelial cells, colored by normal and malignant cells. The *Right* plot showing the distribution of CNV scores for normal and malignant epithelial cell cluster. (*G*) UMAP plot showing four malignant epithelial clusters (MC1–MC4) colored by their tissue of origin (primary CRC or liver metastasis). (*H*) UMAP plot showing four malignant epithelial clusters colored by CytoTRACE scores. The *Right* box plots compared CytoTRACE scores between the four malignant clusters, with TFF3+MC4 showing the highest differential potential. (*I*) Heatmap displaying the expression of stemness-related genes and AUCell scores for stem cell–related processes across the four malignant clusters. (*J*) Gene ontology (GO) enrichment analysis for each malignant cluster. (*K*) The semisupervised trajectory of malignant cells using Monocle, visualizingg pseudotime (*Top*), cell clusters (*Middle*), and tissue sources (*Bottom*). (*L*) Expression patterns of S100A2 and TFF3 along the pseudotime trajectory. (*M*) Heatmap showing the temporal expression of stemness and EMT-related genes along the pseudotime trajectory. (*N*) The spatial distribution of TFF3+MC4 cells in spatial transcriptomics data. (*O*) Heatmap showing the tissue distribution of TFF3+MC4 cells by Ro/e score. Ro/e >1, +++; 1 >or= Ro/e > 0.8, ++; 0.8 > or= Ro/e > 0.2, +; 0.2 >or= Ro/e > 0, ±; Ro/e = 0, −. (*P*) Kaplan–Meier survival curves showing overall survival in TCGA-CRC and GSE159216. (*Q*) Gene set enrichment analysis (GSEA) based on the genes ranked by the relationship with TFF3+MC4 score.

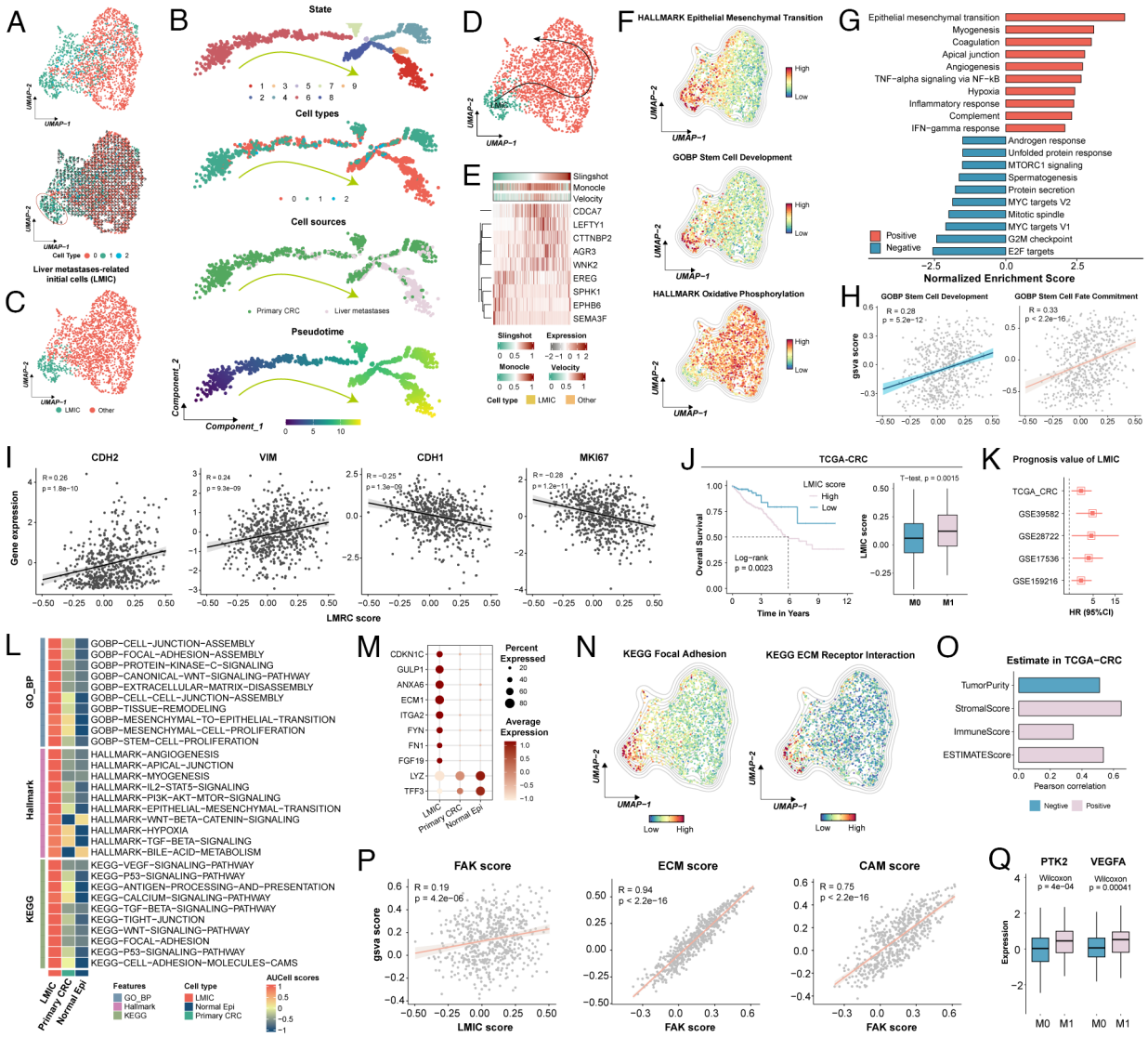


Fig. 2. Identification of Liver Metastasis-Initialing Cells (LMICs) in Primary CRC Tissues. (*A*) UMAP plots showing the reclustering of TFF3+MC4 cells (*Top*) and VECTOR analysis results for the developmental sequence of TFF3+MC4 cells in CRC liver metastasis (*Bottom*). (*B*) Trajectory plot showing the timing sequence of tumor cell development colored by state (*Top*), cell types (middle top), sources (*Middle* down), and pseudotime (*Bottom*). (*C*) UMAP plot showing the LMICs, identified based on both VECTOR and Monocle algorithms. (*D*) UMAP plot showing the Slingshot pseudotime trajectory further validated the lineage relationship of the identified LMICs, positioning them at the beginning of the inferred developmental trajectory. (*E*) Heatmap of key genes across the LMICs. CDCA7 and LEFTY1 increasing and others like SEMA3F and SPHK1 decreasing as cells progress through the differentiation trajectory. (*F*) UMAP plots showing AUCell scores for EMT stem cell development and oxidative phosphorylation pathways. (*G*) GSEA results showing positive and negative correlations of LMIC score with pathway activities. (*H*) Scatter plots demonstrating correlations between LMIC score and stemness-related pathways. (*I*) Scatter plots showing the relationship between LMIC score and markers of epithelial (CDH1), mesenchymal (CDH2, VIM), and proliferation (MKI67). (*J*) Kaplan–Meier survival curves from the TCGA-CRC dataset showing that patients with higher LMIC score had worse overall survival compared to those with lower LMIC score. (*K*) COX analysis across multiple CRC datasets, showing that the LMIC score is associated with increased poor prognosis risk. (*L*) Heatmap of GO, KEGG, and hallmark pathway showing the biological characteristics of LMICs compared to other CRC cell populations. (*M*) Dot plot showing the expression of key genes (e.g., ECM1, FYN) in LMICs. (*N*) UMAP plots showing focal adhesion and ECM–receptor interaction pathway activities. (*O*) Bar plot showing ESTIMATE stromal and immune scores in TCGA-CRC. (*P*) Scatter plots showing significant correlations between LMIC score and focal adhesion (FAK), ECM, and cell adhesion molecule (CAM) pathway activities. (*Q*) Box plots showing increased expression of PTK2 (a key kinase in the FAK pathway) and VEGFA (a downstream target of FAK) in metastatic (M1) versus non-metastatic (M0) patients.

acid metabolism (Fig. 6*E*). Given the established role of MAPK in oncogenic signaling, we further investigated four specific MAPK-related pathways, analyzing differential gene expression between the treatment groups. Heatmap analysis demonstrated coordinated upregulation of p38 and JNK pathway components (Fig. 6*F*). Consistent with these observations, GSEA in TCGA-CRC confirmed the activation of MAPK pathway related to SEMA3C (*SI Appendix*, Fig. S9*B*). Furthermore, MAPK-p38 and MAPK-JNK pathway activity scores were calculated, showing a significant positive correlation with SEMA3C expression level (Fig. 6*G*). IHC and mIHC staining showed that CAF–Sema3c group exhibited stronger p-p38 staining signals, and colocalization of p-p38 (red) and EPCAM (green) indicated p38 activation specifically within tumor cells (Fig. 6*H*). Western blotting analysis (Fig. 6 *I* and *K*) further substantiated that rhSEMA3C treatment enhanced p38 and JNK phosphorylation in tumor cells, which was accompanied by increased expression of mesenchymal markers Vimentin, N-cadherin, and ZEB1, alongside reduced expression of the epithelial marker E-cadherin. Importantly, these effects were significantly attenuated by NRP2 knockdown, indicating that SEMA3C predominantly activates the MAPK-p38/JNK pathways via the NRP2 receptor. Inhibition of p38/JNK signaling (LL-Z1640-4) significantly attenuated SEMA3C-induced migratory and invasive capacities

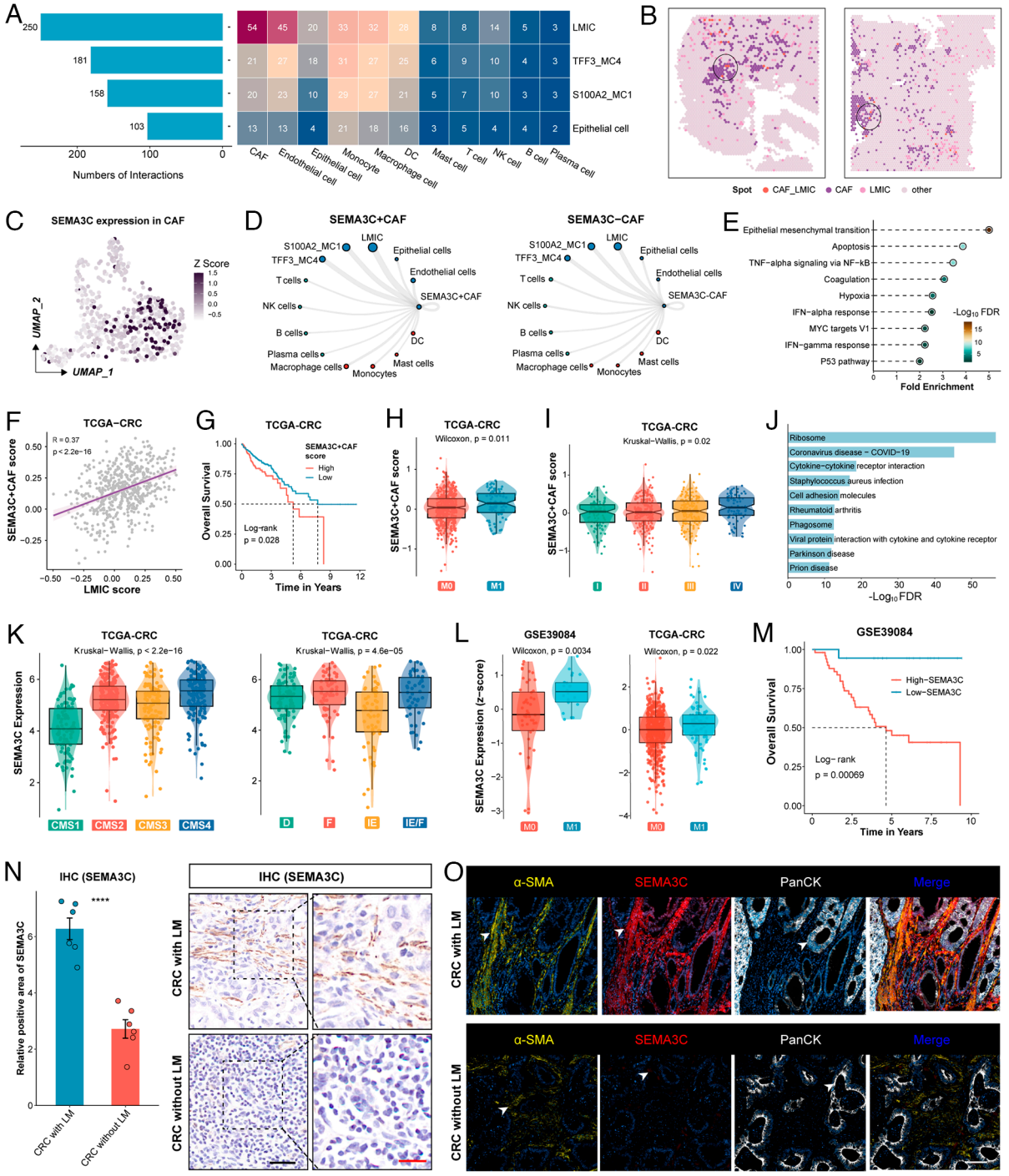


Fig. 3. CAF–LMIC Interactions Promote Liver Metastasis via the SEMA3C–NRP2 Ligand–Receptor Axis. (*A*) Bar plot showing the number of cell–cell interactions between LMICs and various cells in TME via CellPhoneDB. LMIC exhibits the highest number of interactions with CAF. The heatmap on the *Right* highlights the interaction patterns between LMICs and different cell types, with LMIC–CAF interactions being the most prominent. (*B*) Spatial transcriptomics showing the spatial proximity of LMICs and CAFs. Spots colocalized with LMIC and CAFs, only CAFs, and only LMICs are shown in the different colors. (*C*) UMAP plot showing the expression of SEMA3C in CAFs. (*D*) Network plots illustrating cell–cell communication between CAFs and other cell types. SEMA3C+CAFs exhibits more interactions with other cell types than SEMA3C–CAFs and exhibits the strongest interactions with LMICs. (*E*) Function enrichment analysis showing pathways highly enriched in SEMA3C+ CAFs, including EMT, apoptosis, and cytokine–receptor interactions. (*F*) Scatter plot showing a positive correlation between SEMA3C+CAFs score and LMIC score in TCGA-CRC. (*G*) Kaplan–Meier survival curves showing that CRC patients with higher SEMA3C+CAFs score is associated with worse OS in TCGA-CRC. (*H*) Box plot showing the correlation between SEMA3C+CAF score and tumor stages in TCGA-CRC, indicating a higher score in patients with distant metastasis. (*I*) Box plot comparing SEMA3C+CAF score across different lymph node stages, indicating increased SEMA3C+CAFs activity in higher stages. (*J*) GSEA for genes highly correlated with SEMA3C+CAFs, showing enrichment for cytokine–receptor interaction, focal adhesion, and CAM pathways. (*K*) Box plots showing SEMA3C expression across CRC subtypes (CMS1-CMS4) and molecular subtypes (Desert, D; Fibrotic, F; Immune-Enriched, Non-Fibrotic, IE; Immune-Enriched, Fibrotic, IE/F). CMS4 and subtype F, both stromal-enriched subtypes, exhibit significantly higher SEMA3C expression. (*L*) Box plots comparing SEMA3C expression in metastatic and nonmetastatic samples from the GSE39084 and TCGA-CRC cohort, showing significantly higher expression in samples with distant metastasis. (*M*) Kaplan–Meier survival curve from GSE39084 showing that higher SEMA3C expression is associated with worse OS. (*N*) IHC images showing the SEMA3C expression in CRC tissue. Intense staining of SEMA3C is observed in CRC with liver metastasis (LM) compared to those without LM. The bar plot showing the quantitative analysis of IHC, revealing a significantly higher relative positive area of SEMA3C in CRC patients with LM compared to those without LM (P <0.05). Scale bars, black (100 μm) or red (50 μm). (*O*) mIHC assays showing the colocalization of α-SMA (CAF marker), SEMA3C, and PanCK (epithelial marker) in CRC samples with and without LM. (Scale bar, 100 μm.)

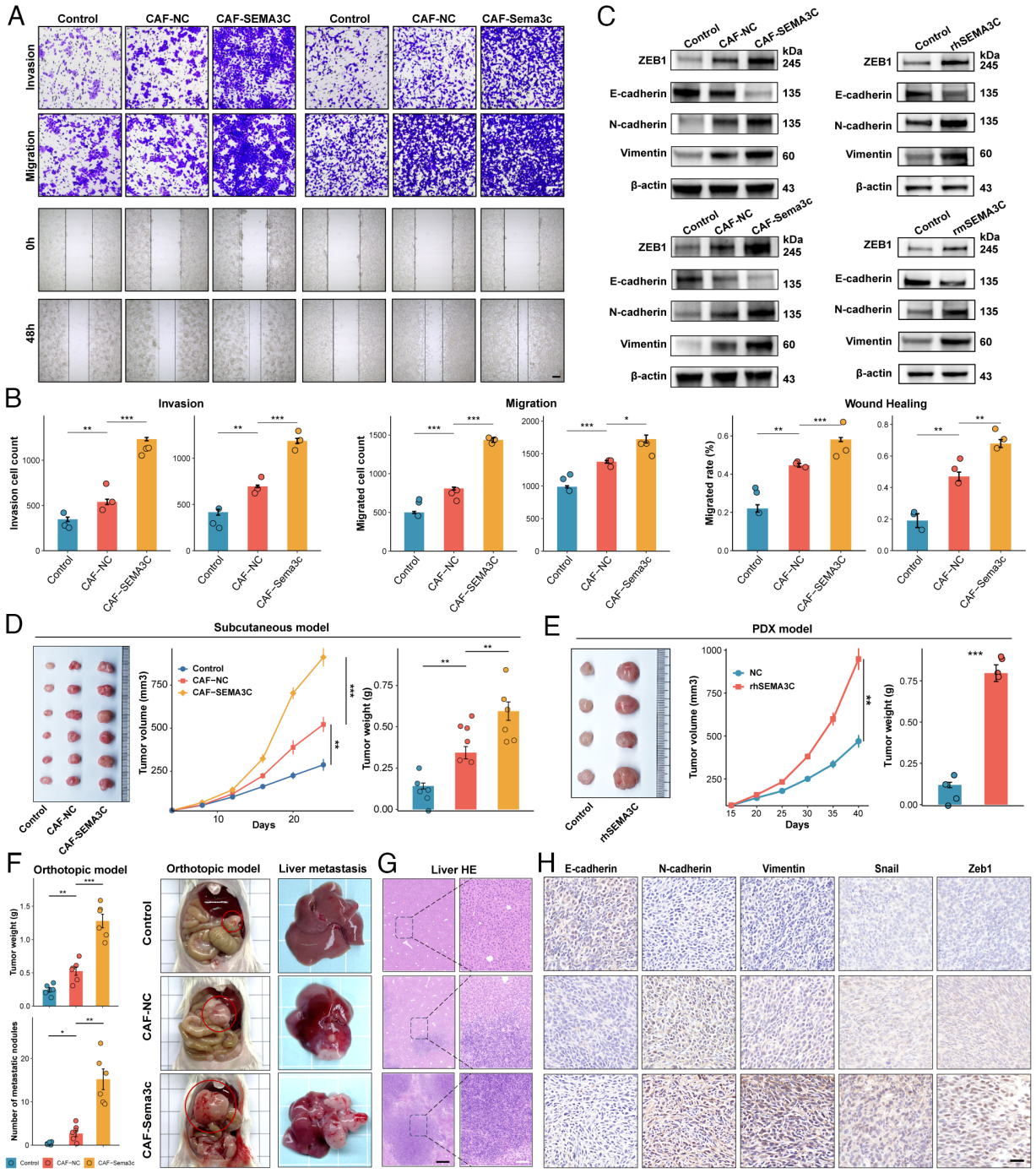


Fig. 4. CAF-secreted SEMA3C Promotes Liver Metastasis and Poor Prognosis in CRC. (*A*) Transwell assays and wound healing assays in SW480 and CT26 cells only or treated with CAF–NC CM, and CAF–SEMA3C/CAF–Sema3c CM. The results showing that CAF–SEMA3C or CAF–Sema3c significantly promotes the invasion and migration ability of SW480 and CT26 cells compared with CAF–NC. Scale bars, white (100 μm) or black (200 μm). (*B*) Quantification of the invasion, migration, and wound healing assays in SW480 cells and CT26 cells only or treated with CM from CAF–NC or CAF–SEMA3C/CAF–Sema3c. (*C*) Western blotting assay of EMT-related proteins (ZEB1, N-cadherin, E-cadherin, and Vimentin) from SW480 only or treated with CAF–NC CM, CAF–SEMA3C CM or rhSEMA3C, and CT26 only or treated with CAF–NC CM, CAF–Sema3c CM or rmSEMA3C. (*D*) Tumor volume growth curves and tumor weight in subcutaneous tumor model treated with tumor cells only (n = 6), CAF–SEMA3C (n = 6), and CAF–NC (n = 6). Tumors in the CAF–SEMA3C group exhibit significantly larger volumes and weights than CAF–NC group. (*E*) Tumor volume growth curves and tumor weight in a patient-derived xenograft (PDX) model treated with rhSEMA3C (n = 4) versus control (n = 4). Mice treated with rhSEMA3C showing significantly larger tumor volumes and weights than controls. (*F*) Liver metastatic lesions and orthotopic primary tumors were collected from an orthotopic liver metastasis mouse model across three group: CT26 cells only (control, n = 6), CT26 coinjected with CAF–NC (n = 6), or CT26 coinjected with CAF–Sema3c (n = 6). Quantification of tumor weight showing a significantly larger tumor mass in the CAF–Sema3c group compared to CAF–NC, and CAF–NC compared to CT26 cells only. Quantification of the number of liver metastasis in three groups. (*G*) HE images of liver from mice injecting CT26 only or coinjecting CT26 cells with either CAF–NC or CAF–Sema3c. Scale bars, black (500 μm) or white (100 μm). (*H*) IHC staining for EMT-related protein (E-cadherin, N-cadherin, Vimentin, Snail, and Zeb1) in tumors from mice injecting CT26 cells only or coinjecting CT26 cells with either CAF–NC or CAF–Sema3c. (Scale bar, 100 μm.)

(Fig. 6 *J* and *K*). These indicated that SEMA3C enhanced tumor cell invasion by activating the MAPK-p38/JNK pathways. Finally, a schematic diagram summarizing the proposed mechanism was provided (Fig. 6*L*).

Discussion

Despite improved overall survival through enhanced surveillance and treatment strategies, clinical outcomes for CRC patients

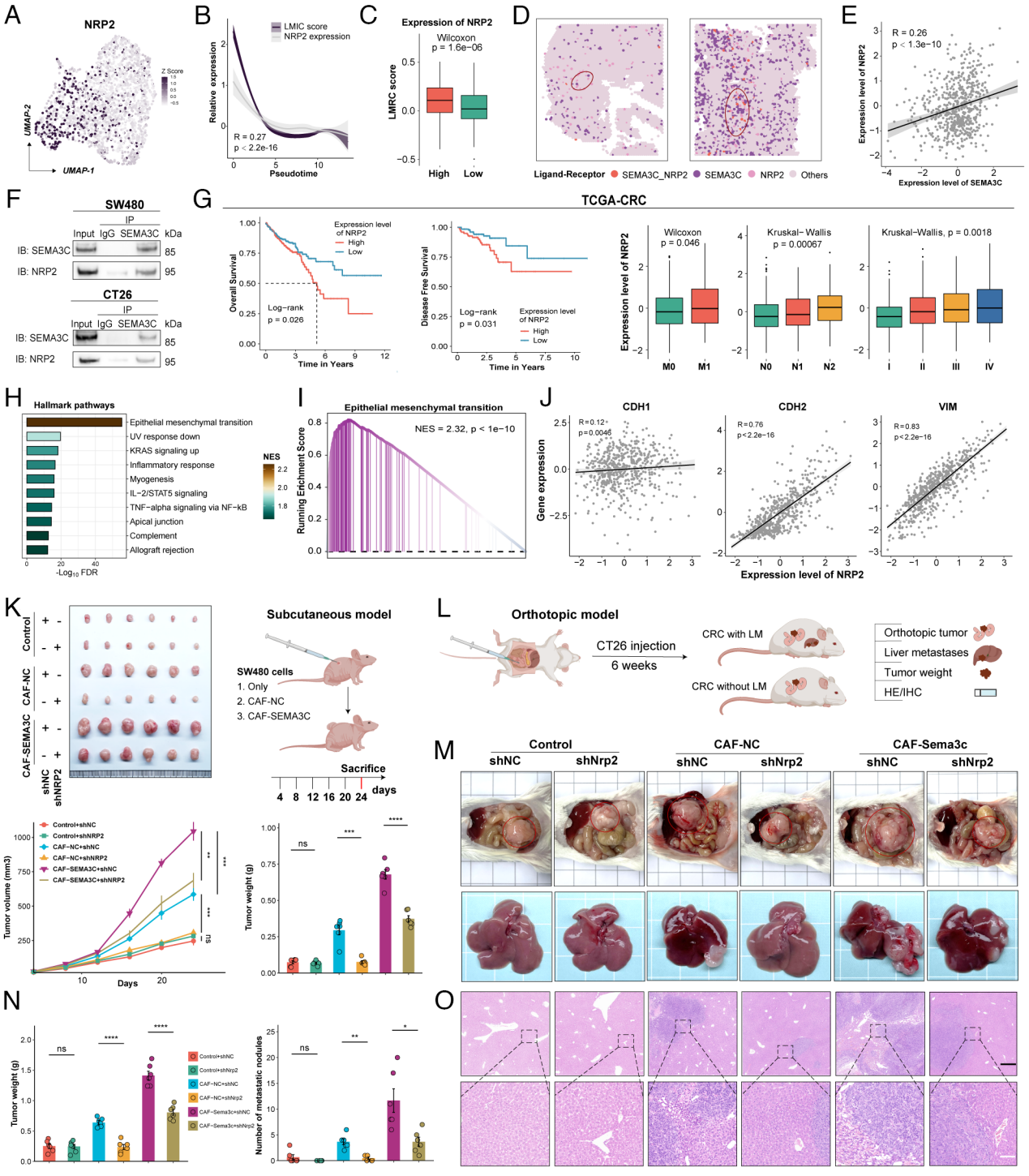


Fig. 5. SEMA3C Mediates Liver Metastasis via Direct Interaction with NRP2. (*A*) UMAP plot showing NRP2 expression in LMICs. NRP2 is specifically expressed in LMICs, with overlapping distribution patterns between NRP2 and LMICs. (*B*) Correlation analysis showing strong positive correlations between NRP2 expression and LMIC score. (*C*) Box plot showing that higher NRP2 expression correlates with increased LMIC score in TCGA-CRC. (*D*) Spatial transcriptomics analysis depicting the colocalization of SEMA3C and NRP2. Ligand–receptor pairs are highlighted. (*E*) Scatter plot showing a positive correlation between SEMA3C and NRP2 expression in TCGA-CRC. (*F*) COIP assays confirming the physical interaction between SEMA3C and NRP2 in SW480 and CT26 cell lines. (*G*) Kaplan–Meier survival curves showing patients with higher NRP2 expression have significantly worse OS (*Left*) and disease-free survival (DFS) (*Right*). Box plots showing that higher NRP2 expression correlates with metastasis (*Left*), lymph node metastasis (*Middle*), and advanced tumor stages (*Right*). (*H* and *I*) GSEA showing that high SEMA3C expression is associated with activation of EMT and other metastasis-related pathways. (*J*) The scatter plot showing a positive correlation between NRP2 expression and EMT markers (CDH1, CDH2, VIM). NRP2 shows a strong positive correlation with mesenchymal markers (CDH2 and VIM), while the correlation with the epithelial marker (CDH1) is weak. (*K*) In vivo tumor growth assays in a subcutaneous mouse model. CAF–SEMA3C group developing larger tumors, and this effect is reversed by shNRP2. Tumor volume and weight are significantly reduced in mice injected with shNRP2 cells compared to controls. (*L*) Flowchart of orthotopic tumor model construction and subsequent processing. (*M–O*) In vivo orthotopic liver metastatic model using CT26 cells. Mice coinjecting with CT26 cells and CAF–Sema3c exhibiting increased tumor growth and liver metastasis, while shNRP2 reverses the enhanced tumor growth and liver metastasis. Images of orthotopic model and liver metastasis (*M*), quantality analysis (*N*), and HE (*O*) confirm that NRP2 knockout reduces liver metastasis. Scale bars, black (500 μm) or white (100 μm).

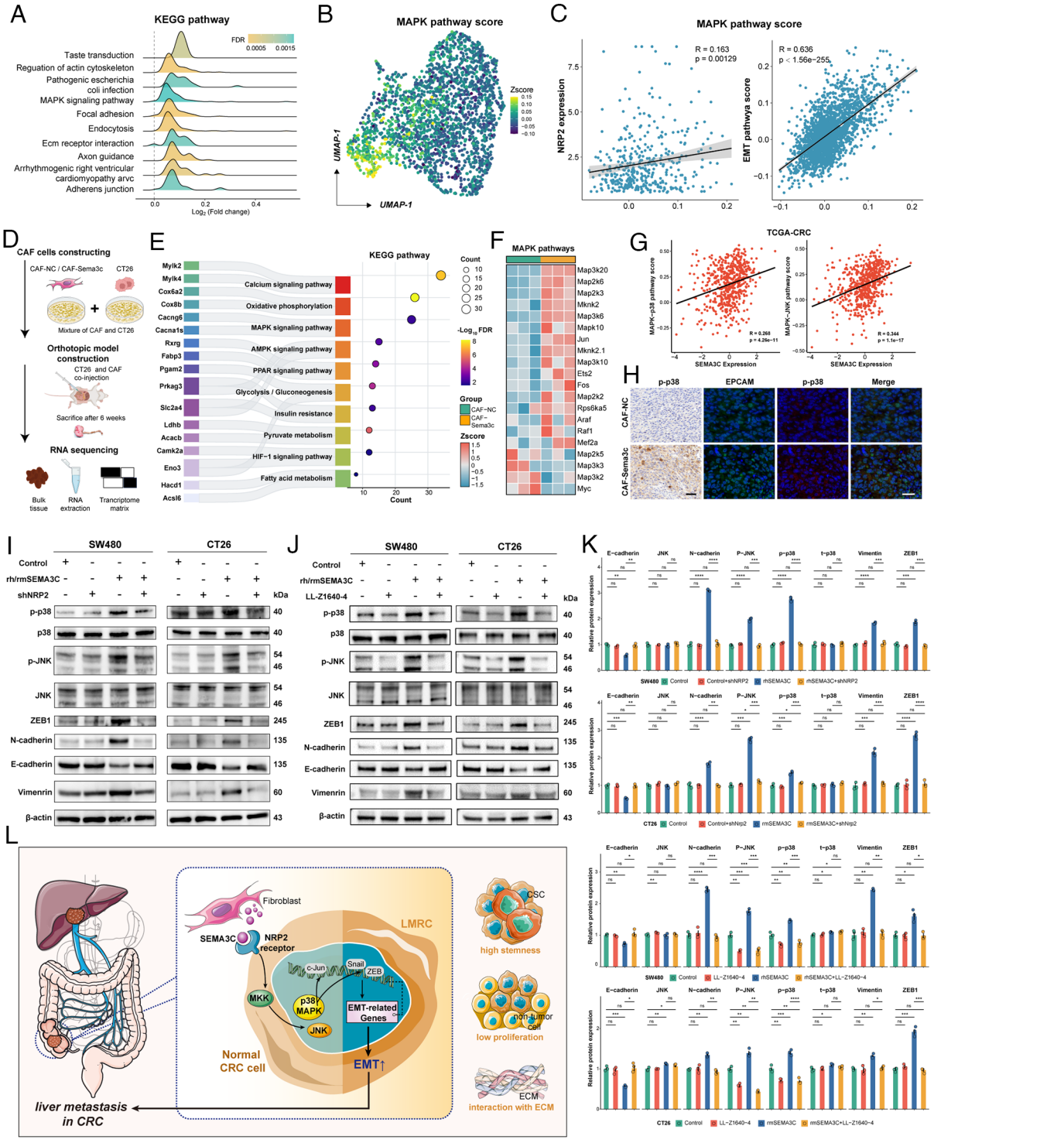


Fig. 6. SEMA3C Promotes Liver Metastasis via NRP2-mediated MAPK activation. (*A*) Functional enrichment analysis of NRP2+ malignant cells showing significant activation of the MAPK signaling pathway and other tumor-related pathways, including regulation of actin cytoskeleton, focal adhesion, and ECM–receptor interactions. (*B*) UMAP plot showing the MAPK pathway activity score. Cells within the LMICs region exhibit significantly higher MAPK pathway activity. (*C*) Scatter plots showing positive correlations between MAPK pathway scores and NRP2 expression (*Left*) and MAPK pathway scores and EMT pathway activity (*Right*) in TCGA-CRC. (*D*) Schematic diagram of the experimental design. CT26 cells are coinjected with CAF–NC or CAF–Sema3c cells. After 6 wk of growth in an orthotopic mouse model, tumors are harvested for RNA sequencing. (*E*) KEGG pathway enrichment analysis of the transcriptomic data from CAF–Sema3c group, highlighting significant activation of tumor-related pathways, including MAPK, HIF-1, and fatty acid metabolism. (*F*) Heatmap showing the expression of key genes in the MAPK-p38 and MAPK-JNK pathways, with significant upregulation of MAP3K20 and other upstream regulators in CAF–SEMA3C group. (*G*) Scatter plots showing the correlation between SEMA3C expression and MAPK-p38 as well as MAPK-JNK pathway score. (*H*) IHC and mIHC analysis of p-p38 expression and colocalization with EPCAM in tumor tissues. mIHC of p-p38 (red) and EPCAM (green) in tumor tissues from CAF–Sema3c and CAF–NC groups. Colocalization of p-p38 and EPCAM indicates p38 activation specifically within epithelial tumor cells. Scale bars, black (100 μm) or white (50 μm). (*I*) Western blotting assays of SW480 and CT26 cells treated with recombinant SEMA3C protein and shNRP2. Recombinant SEMA3C protein increases phosphorylation of p38 and JNK, upregulates ZEB1, N-cadherin, and Vimentin, and downregulates E-cadherin. These effects are significantly reversed by shNRP2, indicating the role of the SEMA3C–NRP2 axis in MAPK-p38 and JNK activation. (*J*) Western blotting assays of SW480 and CT26 cells treated with recombinant SEMA3C protein and the p38/JNK inhibitor (LL-Z1640-4). Recombinant SEMA3C protein increases phosphorylation of p38 and JNK, upregulates ZEB1, N-cadherin, and Vimentin, and downregulates E-cadherin. Inhibition of p38/JNK signaling significantly reduced the phosphorylation levels of p38 and JNK. (*K*) Quantitative analysis of Western blotting assays. (*L*) Schematic model illustrating the proposed mechanism by which SEMA3C promotes CRC liver metastasis. SEMA3C secreted by CAFs interacts with NRP2 on tumor cells, activating the MAPK signaling pathway and promoting EMT, leading to CRC progression and liver metastasis.

remain suboptimal, largely attributed to frequent liver metastasis development (24). While surgical resection remains the primary curative approach for liver metastasis (1), effective early-stage therapeutic interventions are critically needed. Accumulating evidence indicates that metastasis initiation and maintenance are driven by stem-like cell subpopulations at primary tumor sites, as evidenced in ovarian cancer and lung adenocarcinoma (5, 6). However, the identity and functional characteristics of metastasis-initiating cells in CRC remain poorly characterized. Here, we employed three temporally resolved analytical approaches to identify LMICs as key mediators of CRC liver metastasis and unveil the SEMA3C–NRP2–MAPK axis as a promising therapeutic target for preventing metastatic progression.

The disruption and remodeling of the tumor immune microenvironment influence tumor cell invasion, metastasis, and therapeutic resistance through biochemical and physical signals (25). Our findings demonstrate that targeting the SEMA3C–NRP2 axis suppresses LMIC-driven invasive signaling, offering a therapeutic approach for early intervention in CRC liver metastasis. Although SEMA3C plays a pivotal role in stromal remodeling and tumor-stromal communication, its direct therapeutic targeting is hindered by challenges including low specificity, poor localization, and difficulty in sustaining effective drug concentrations. In contrast, NRP2, as a specific marker of LMICs, provides a more precise therapeutic target. Intervention via NRP2 or its downstream effectors provides a tailored strategy to block CRC liver metastasis progression. We further demonstrated that the SEMA3C–NRP2 interaction activates the MAPK-p38/JNK pathway, which subsequently upregulates the expression of EMT-related molecules. Activation of the p38 and JNK pathways not only induces EMT-associated transcription factors, leading to the loss of tumor cell polarity, but also enhances cell migratory capacity and matrix degradation ability (26). Previous studies have emphasized the critical role of p38 pathway activation in endowing tumor cells with invasive capabilities, with p38 inhibition significantly reducing metastasis in hepatocellular carcinoma (27), head and neck squamous carcinoma (28), melanoma (29), and lung cancer (30). Although the JNK pathway is implicated in tumor metastasis, the functional links between JNK-dependent targets (e.g., MMPs and inflammatory cytokines) and cancer progression remain incompletely characterized in experimental models. Additionally, as classic MAPK pathways, p38 and JNK frequently interact during cellular regulation, often in a context-dependent manner (26).

Although we identified LMICs in single-cell data and defined their functional roles and clinical relevance, precise characterization of this cellular subset necessitates further validation. Furthermore, the MAPK pathway exhibits multifaceted regulatory control over cell fate determination. However, functional redundancy and extensive crosstalk among these pathways pose technical challenges in comprehensively delineating their interplay. Consequently, pharmacological inhibition of the MAPK pathway alone proves insufficient to abrogate the metastatic capacity of LMICs, underscoring the need for combinatorial therapeutic strategies.

In conclusion, our study identified a subpopulation of tumor cells, termed LMICs, exert a critical role during liver metastasis. These cells exhibit stem cell–like properties, low proliferative capacity, and strong interactions with the ECM, especially CAFs in the TME. CRC patients with a dominance of SEMA3C+CAFs exhibited liver metastasis and poor prognosis, highlighting its potential as a biomarker for CRC liver metastasis. Furthermore, we demonstrated that CAF-secreted SEMA3C binds to the NRP2 receptor, activating the MAPK-p38/JNK signaling pathway, promoting an invasive tumor phenotype, and driving CRC liver metastasis. These findings establish the SEMA3C–NRP2/MAPK axis as a therapeutically targetable pathway, providing a rationale for combined inhibition strategies to suppress metastatic progression in CRC.

Materials and Methods

scRNA-Seq Data Preprocessing. The scRNA-seq datasets were used in this study to identify and evaluate the liver metastasis-related initial cells, including data by Sathe et al. (31) and Liheng et al. (GSE178318) (32). Quality control was uniformly applied to each single-cell cohort as follows: 1) The raw gene expression matrix of each single-cell dataset was converted into a Seurat object using the R package Seurat (v4.4.0); 2) Doublets were removed from each sample using the R package DoubletFinder (v2.0.3) (33); 3) Novelty scores were calculated by determining the ratio of nFeature to nCount to assess the complexity of RNA species in each cell; 4) Cells with nFeature less than 200 or greater than 5,000, nCount less than 500 or greater than 40,000, Novelty scores greater than 0.8, or mitochondrial gene content exceeding 10% were classified as low-quality cells and subsequently removed; 5) Genes expressed in fewer than 5 cells were also removed; 6) Samples with more than 2,000 cells after quality control remained.

Following quality control, cohorts were combined and the harmony R package corrected the batch effects (34). SCTransform function normalized the data and the top 30 principal components (PCs) with a resolution of 2.0 for clustering. Cell clusters were identified using the FindClusters function and annotated based on typical markers of different cell types collected from literature (31, 32, 35). The InferCNV R package was used to identify malignant cells with the parameters: "denoise", default hidden Markov model (HMM) settings, cutoff 1 for Smart-seq = 2, or cutoff = 0.1 for 10x Genomics. The stromal cells including the endothelial and fibroblast cells were used as a normal reference (19).

Isolation of Primary Human or Mouse CAFs. Fresh human colon cancer tissues were collected from patients at the First Affiliated Hospital of Zhengzhou University. All participants provided written informed consent in accordance with the Declaration of Helsinki. Ethical approval was confirmed by the Ethics Committee of Zhengzhou University (ZZUIRB 2023-320). Colon cancer tissues free from contamination were washed several times with 5 × trypsin PBS (Servicebio, Wuhan, China) until the PBS was clarified, removing fat and necrotic tissues. The tissues were then cut into 1 mm^3 small pieces and digested with 1 mg/mL type IV collagenase (Thermo Scientific, Shanghai, China) at 37 °C for 2 h. After centrifugation to remove the supernatant and filtration through a 200-mesh filter, the tissues were resuspended in DMEM high glucose culture medium containing 10% fetal bovine serum and seeded into 6 cm cell culture dishes. After 72 h, the culture medium was replaced to remove nonadherent cells. Mouse colon cancer tissues were obtained from in situ tumors constructed with CT26 cells in mice, and mouse CAFs were isolated using the same procedure.

In vivo PDX Mouse Model. 4-wk-old male C-NKG mice were obtained from Cyagen Biosciences Inc. (Suzhou, China). Fresh colorectal cancer tumor samples from patients were diced into 2 mm^3 pieces and implanted subcutaneously into the right flank of the NSG mice. Tumor growth was monitored regularly. When the tumors reached a sufficient size, they were excised, cut into 2 mm^3 pieces, and reimplanted into a new group of NSG mice. Once the tumors grew to a volume of 100 mm^3, the mice were randomly assigned to different treatment groups. Body weight was recorded every 5 d, and tumor volume was calculated using the formula: 0.5 × length × $width^2$. All animal procedures were conducted in compliance with the guidelines approved by the Institutional Animal Care and Use Committee of Zhengzhou University.

Statistical Analysis. All data processing, statistical analysis, and plotting were performed using R 4.3.2. Pearson's correlation coefficients assessed correlations between continuous variables. The chi-squared test compared categorical variables, while the Wilcoxon rank-sum test or *t* test compared continuous variables. The survminer package determined the optimal cut-off values. Cox regression and Kaplan–Meier analyses were conducted using the survival package. All statistical tests were two-sided, with $P < 0.05$ considered statistically significant. Detailed experimental protocols and analytical workflows are described in *SI Appendix, Supplementary Methods*.

Data, Materials, and Software Availability. All scRNA-seq datasets used in this study are publicly available. The datasets can be accessed via the following links: JIRGSU (https://dna-discovery.stanford.edu/research/datasets/) (32),

GSE178318 (https://www.ncbi.nlm.nih.gov/geo/query/acc.cgi?acc=GSE178318) (32). Additionally, the 10X Visium Spatial transcriptome data were retrieved from the scCRLM atlas (http://www.cancerdiversity.asia/scCRLM/) (36). All other data are included in the manuscript and/or *SI Appendix*.

ACKNOWLEDGMENTS. This study was supported by grants from Henan Medical Science and Technology Research Plan (LHG120230294), The China Postdoctoral Science Foundation (2023M743201), the National funded post-doctoral researcher program (GZB20230671), and the National Natural Science Foundation of China (8240114555).

Author affiliations: [a]Department of Interventional Radiology, The First Affiliated Hospital of Zhengzhou University, Zhengzhou 450052, Henan, China; [b]Interventional Institute of Zhengzhou University, Zhengzhou 450052, Henan, China; [c]Interventional Treatment and Clinical Research Center of Henan Province, Zhengzhou 450052, Henan, China; [d]Department of Clinical Medicine, Zhengzhou University, Zhengzhou 450052, Henan, China; [e]Department of Colorectal Surgery, The First Affiliated Hospital of Zhengzhou University, Zhengzhou 450052, Henan, China; [f]Department of Oncology, Zhujiang Hospital, Southern Medical University, Guangzhou 510515, China; [g]Department of Neurosurgery, Xiangya Hospital, Central South University, Changsha 410000, China; [h]Department of Radiation Oncology, Zhongshan Hospital, Fudan University, Shanghai 200032, China; [i]Tianjian Laboratory of Advanced Biomedical Sciences, Academy of Medical Sciences, Zhengzhou University, Zhengzhou 450052, Henan, China; [j]Department of Oncology, The First Affiliated Hospital of Zhengzhou University, Zhengzhou 450052, Henan, China; and [k]Institute of Basic Medical Sciences, Chinese Academy of Medical Sciences and Peking Union Medical College, Beijing 100730, China

1. X. Shi *et al.*, Mechanism insights and therapeutic intervention of tumor metastasis: Latest developments and perspectives. *Signal Transduct. Target Ther.* **9**, 192 (2024).
2. K. Ganesh, J. Massagué, Targeting metastatic cancer. *Nat. Med.* **27**, 34–44 (2021).
3. S. Milette *et al.*, Molecular pathways: Targeting the microenvironment of liver metastases. *Clin. Cancer Res.* **23**, 6390–6399 (2017).
4. A. Cañellas-Socias *et al.*, Metastatic recurrence in colorectal cancer arises from residual EMP1(+) cells. *Nature* **611**, 603–613 (2022).
5. Z. Wang *et al.*, Single-cell transcriptomic analyses provide insights into the cellular origins and drivers of brain metastasis from lung adenocarcinoma. *Neuro. Oncol.* **25**, 1262–1274 (2023).
6. T. Kan *et al.*, Single-cell RNA-seq recognized the initiator of epithelial ovarian cancer recurrence. *Oncogene* **41**, 895–906 (2022).
7. E. Sahai *et al.*, A framework for advancing our understanding of cancer-associated fibroblasts. *Nat. Rev. Cancer* **20**, 174–186 (2020).
8. Y. Chhabra, A. T. Weeraratna, Fibroblasts in cancer: Unity in heterogeneity. *Cell* **186**, 1580–1609 (2023).
9. K. E. de Visser, J. A. Joyce, The evolving tumor microenvironment: From cancer initiation to metastatic outgrowth. *Cancer Cell* **41**, 374–403 (2023).
10. V. Aggarwal *et al.*, Interplay between tumor microenvironment and partial EMT as the driver of tumor progression. *iScience* **24**, 102113 (2021).
11. A. P. Patel *et al.*, Single-cell RNA-seq highlights intratumoral heterogeneity in primary glioblastoma. *Science* **344**, 1396–401 (2014).
12. G. S. Gulati *et al.*, Single-cell transcriptional diversity is a hallmark of developmental potential. *Science* **367**, 405–411 (2020).
13. C. Trapnell *et al.*, The dynamics and regulators of cell fate decisions are revealed by pseudotemporal ordering of single cells. *Nat. Biotechnol.* **32**, 381–386 (2014).
14. Q. Zhang *et al.*, Landscape and dynamics of single immune cells in hepatocellular carcinoma. *Cell* **179**, 829–845.e20 (2019).
15. F. Zhang, X. Li, W. Tian, Unsupervised inference of developmental directions for single cells using VECTOR. *Cell Rep* **32**, 108069 (2020).
16. K. Street *et al.*, Slingshot: Cell lineage and pseudotime inference for single-cell transcriptomics. *BMC Genomics* **19**, 477 (2018).
17. M. Efremova *et al.*, Cell PhoneDB: Inferring cell-cell communication from combined expression of multi-subunit ligand-receptor complexes. *Nat. Protoc.* **15**, 1484–1506 (2020).
18. X. Xu *et al.*, Increased semaphorin 3c expression promotes tumor growth and metastasis in pancreatic ductal adenocarcinoma by activating the ERK1/2 signaling pathway. *Cancer Lett.* **397**, 12–22 (2017).
19. J. W. Peacock *et al.*, SEMA3C drives cancer growth by transactivating multiple receptor tyrosine kinases via Plexin B1. *EMBO Mol. Med.* **10**, 219–238 (2018).
20. H. Peng *et al.*, Semaphorin 3C (Sema3C) reshapes stromal microenvironment to promote hepatocellular carcinoma progression. *Signal Transduct. Target Ther.* **9**, 169 (2024).
21. Z. Liu *et al.*, BEST: A web application for comprehensive biomarker exploration on large-scale data in solid tumors. *J. Big Data* **10**, 165 (2023).
22. J. Guinney *et al.*, The consensus molecular subtypes of colorectal cancer. *Nat. Med.* **21**, 1350–6 (2015).
23. A. Bagaev *et al.*, Conserved pan-cancer microenvironment subtypes predict response to immunotherapy. *Cancer Cell* **39**, 845–865.e7 (2021).
24. Y. Wang *et al.*, Liver metastasis from colorectal cancer: Pathogenetic development, immune landscape of the tumor microenvironment and therapeutic approaches. *J. Exp. Clin. Cancer Res.* **42**, 177 (2023).
25. A. L. Correia, Locally sourced: Site-specific immune barriers to metastasis. *Nat. Rev. Immunol.* **23**, 522–538 (2023).
26. E. F. Wagner, A. R. Nebreda, Signal integration by JNK and p38 MAPK pathways in cancer development. *Nat. Rev. Cancer* **9**, 537–549 (2009).
27. Y. H. Hsieh *et al.*, p38 mitogen-activated protein kinase pathway is involved in protein kinase Calpha-regulated invasion in human hepatocellular carcinoma cells. *Cancer Res.* **67**, 4320–7 (2007).
28. C. Liu *et al.*, Cannabinoids promote progression of HPV-positive head and neck squamous cell carcinoma via p38 MAPK activation. *Clin. Cancer Res.* **26**, 2693–2703 (2020).
29. N. Liu *et al.*, Eravacycline improves the efficacy of anti-PD1 immunotherapy via AP1/CCL5 mediated M1 macrophage polarization in melanoma. *Biomaterials* **314**, 122815 (2024).
30. J. Gui *et al.*, Activation of p38α stress-activated protein kinase drives the formation of the pre-metastatic niche in the lungs. *Nat Cancer* **1**, 603–619 (2020).
31. A. Sathe *et al.*, Colorectal cancer metastases in the liver establish immunosuppressive spatial networking between tumor-associated SPP1+ macrophages and fibroblasts. *Clin Cancer Res.* **29**, 244-260 (2022).
32. L. Che *et al.*, A single-cell atlas of liver metastases of colorectal cancer reveals reprogramming of the tumor microenvironment in response to preoperative chemotherapy. *Cell Discov.* **7**, 80 (2021).
33. C. McGinnis *et al.*, DoubletFinder: Doublet detection in single-cell RNA sequencing data using artificial nearest neighbors. *Cell Syst.* **8**, 329–337 (2019).
34. I. Korsunsky *et al.*, Fast, sensitive and accurate integration of single-cell data with Harmony. *Nat. Methods.* **16**, 1289-1296 (2019).
35. H. Lee *et al.*, Lineage-dependent gene expression programs influence the immune landscape of colorectal cancer. *Nat. Genet.* **52**, 594-603 (2020).
36. Y. Wu *et al.*, Spatiotemporal immune landscape of colorectal cancer liver metastasis at single-cell level. *Cancer Discov.* **12**, 134-153 (2022).